applied sciences

MDPI

Article

Effect of Layered Backfill Soil Saturation on Ampacity of Direct-Buried Cables and a Graded Control Strategy

Wenlong Zhang [1] and Ziwei Ma [2,*]

[1] PowerChina Huadong Engineering Corporation Limited, Hangzhou 310030, China; zhang_wl@hdec.com
[2] Faculty of Mechanical and Electrical Engineering, Yunnan Agricultural University, Kunming 650201, China
* Correspondence: 2017022@ynau.edu.cn

Featured Application

The results provide a quantitative basis for saturation-based ampacity control of direct-buried cables in layered red-bed soil backfill, and can be applied directly to the operation and maintenance of distribution networks in Southwest China.

Abstract

IEC 60287 assumes homogeneous soil and static boundaries. This study develops an electro-thermal-fluid FEM model for a 35 kV three-core XLPE cable in layered fine-sand/red-bed-soil backfill, incorporating the Johansen conductivity model with coarse/fine Kersten branches and a sinusoidal irradiance boundary. On a homogeneous baseline, FEM–IEC agreement is within 3.4%. Ampacity rises nonlinearly with saturation degree S_r—increasing by 58.5% from $S_r = 0.1$ to 0.3 and flattening above 0.6. Across seven saturation scenarios, dry red-bed soil ($S_r = 0.3$) reduces ampacity by ~15% relative to wet soil ($S_r = 0.8$), whereas sand desiccation changes it by <2%, identifying red-bed soil as the thermal bottleneck. Increasing the sand layer from 0.1 to 0.7 m improves ampacity by 6.5% at $S_r = 0.1$ but by <1.64% at $S_r \geq 0.4$. Peak solar irradiance on completely dry soil yields the minimum ampacity, with 0–1000 W/m^2 solar loading reducing ampacity by ~20%. A three-tier operational strategy is proposed—normal ($S_{r_red} \geq 0.6$), early warning ($0.3 \leq S_{r_red} < 0.6$), emergency ($S_{r_red} < 0.3$)—with a time-slot derating formula. Because quasi-steady analysis neglects soil thermal inertia, the hourly ampacity ratios are parametric steady-state results rather than an operating schedule, although the daytime peak derating remains conservative. These results overturn the assumption that a water-retaining sand layer ensures thermal safety in Southwest China.

Keywords: ampacity; control strategy; direct-buried cable; dynamic boundaries; finite element method (FEM); layered backfill; saturation; thermal safety

Academic Editor: Andrea Frazzica

Received: 24 October 2026
Revised: 19 November 2026
Accepted: 19 November 2026
Published: 20 November 2026

Copyright: © 2026 by the authors. Licensee MDPI, Basel, Switzerland. This article is an open access article distributed under the terms and conditions of the Creative Commons Attribution (CC BY) license.

1. Introduction

In urban power distribution systems [1], collector networks of photovoltaic (PV) plants and wind farm [2], direct-buried power cables serve as critical infrastructure. Their ampacity and service life depend directly on the temperature field of the cable and its surrounding medium [3,4]. Adverse thermal conditions—including soil properties, burial depth, backfill materials, and solar irradiance—can reduce cable ampacity by up to 40% [5]. Overloading drives excessive conductor temperature, accelerating insulation degradation and shortening service life, whereas operating at unnecessarily low currents wastes asset capacity. Therefore, accurate evaluation of cable temperature fields and am-

pacity is essential for ensuring operational safety, optimizing asset utilization, and extending cable lifespan [6].

At present, cable ampacity evaluation methods fall into three categories: analytical approaches, experimental testing, and the finite element method (FEM). Analytical methods build on the electro-thermal analogy principle to construct thermal-circuit models of steady-state cable ampacity, solving for conductor current through temperature-difference balance equations [7–11]. The accuracy of these methods hinges on precise calculation of thermal resistances across each layer in the circuit; however, they face inherent limitations when applied to asymmetric cable structures and complex laying conditions [12,13].

Experimental approaches determine ampacity by directly loading actual cables and measuring the steady-state conductor temperature response. This method captures real-world thermal-physical processes and naturally accounts for complex factors that idealized models struggle to describe—such as soil moisture migration and backfill material heterogeneity. Nevertheless, experimental testing is costly, time-consuming, and limited in scenario coverage, making it impractical as a general design tool; it is typically reserved for spot-checking critical nodes and model validation [14].

FEM discretizes the cable and surrounding soil into meshes and solves numerically, enabling accurate temperature-field simulation without being constrained by geometric complexity or material inhomogeneity [15–17]. It is widely accepted as a high-fidelity benchmark for evaluating cable ampacity under complicated installation conditions [18–20].

For direct-buried cables, heat dissipates through conduction, convection, and radiation. Consequently, adopting a multiphysics FEM model to simulate the cable thermal field represents the current research trend. Nie et al. [21] developed an electromagnetic-thermal coupling model in COMSOL for XLPE cables under three installation modes—direct burial, conduit, and cable trench—systematically comparing the effects of installation type and cable arrangement on ampacity. Kim et al. [22] employed an electro-thermal-fluid coupled model to investigate how ambient and ground temperatures affect the heat transfer of underground cables embedded in preplaced-aggregate concrete backfill, revealing that seasonal ambient temperature variations significantly influence both cable temperature and ampacity. Hu et al. [23] established an electromagnetic-thermal FEM model for three-core XLPE cables under three-phase unbalanced loading, proposing a correction method for bedding layer thermal resistance that accounts for asymmetric temperature distribution. Zhang et al. [24] built an electromagnetic-thermal-fluid multiphysics model for a 220 kV three-core submarine XLPE AC cable and analyzed how surrounding environmental factors affect the thermal field and ampacity. Since the operating environment of submarine buried cables closely resembles that of land-based direct-buried cables, their computational framework offers a useful reference for terrestrial applications. Chen et al. [25] constructed an electromagnetic-fluid-thermal multiphysics model for a mining cable reel vehicle, studying the temperature rise and heat dissipation characteristics of wound cables; their methodology provides relevant insights for direct-buried cable thermal analysis. Klimenta et al. [26] focused on solar irradiance effects on direct-buried cable ampacity, demonstrating that cool-pavement surfaces can noticeably enhance ampacity. Zhang and Ma [27] applied an electro-thermal-fluid FEM model to examine the influence of burial depth, soil thermal resistivity, solar irradiance, wind speed, and parallel circuit count on ampacity, and proposed a rapid ampacity estimation method based on their simulation results.

Factors affecting direct-buried cable ampacity span soil thermal properties [28,29], environmental conditions [30], and installation practices [31,32]. Among these, soil ther-

mal conductivity, moisture content, drying effects, and layered backfill characteristics are the primary determinants of heat dissipation performance [33]. Yet IEC 60287 neglects practical influences such as surface solar irradiance, convective heat exchange at the ground, and ambient temperature fluctuations. It further simplifies soil as a homogeneous, isotropic medium and disregards the dynamic effect of saturation on soil thermal conductivity, leading to noticeable deviations under realistic complex conditions.

In response to these limitations, researchers have adopted multiphysics coupling models in numerous studies. However, existing models still lack a systematic account of how dynamically varying soil thermal conductivity—driven by saturation changes and moisture migration—affects cable ampacity. Furthermore, most studies assign constant, static values to environmental parameters, failing to capture the diurnal and seasonal variability of actual climate conditions.

To address these gaps, this study takes a 35 kV YJLV22-26/35 3 × 400 three-core cable as the subject and develops an electro-thermal-fluid multiphysics coupling model. It focuses on how spatial saturation distribution in zoned backfill installations and diurnal solar irradiance variation influence the cable temperature field and ampacity, and proposes a control strategy for safe cable operation based on simulation results. This paper extends [27], with the new work primarily focusing on the impact of layered backfill soil structures and spatially distributed saturation on the ampacity of directly buried cables, based on which graded control strategy for cable operation is proposed.

The main contributions of this study are fourfold: (1) A saturation-dependent thermal conductivity model based on the Johansen formula with coarse- and fine-grained Kersten branches is embedded into the FEM governing equations, replacing the conventional homogeneous-soil assumption. (2) The diurnal time-varying characteristics of solar irradiance are incorporated into the boundary conditions, upgrading environmental parameters from static assignments to time-dependent inputs and providing a methodological foundation for ampacity evaluation under more realistic operating conditions. (3) A comparative analysis across four saturation distribution scenarios reveals that redbed soil drying is the dominant constraint on cable heat dissipation, correcting the conventional engineering practice of prioritizing near-cable sand-layer moisture content. (4) A graded operational control strategy with quantitative three-tier saturation thresholds is proposed—normal operation zone ($S_r \geq 0.6$), early-warning zone ($0.3 \leq S_r < 0.6$), and emergency intervention zone ($S_r < 0.3$)—supplying a basis for on-site derating decisions.

This paper is organized as follows: Section 1 reviews existing research; Section 2 describes the computational model and parameter settings; Section 3 presents simulation results and analysis; Section 4 proposes the operational control strategy; and Section 5 concludes the paper.

2. Computation Methods

2.1. Cable Structure and Installations

The structure and electrical parameters of the 35 kV three-core cable YJLV22-26/35 3 × 400 are shown in Figure 1a, and the cable structural parameters are listed in Table 1.

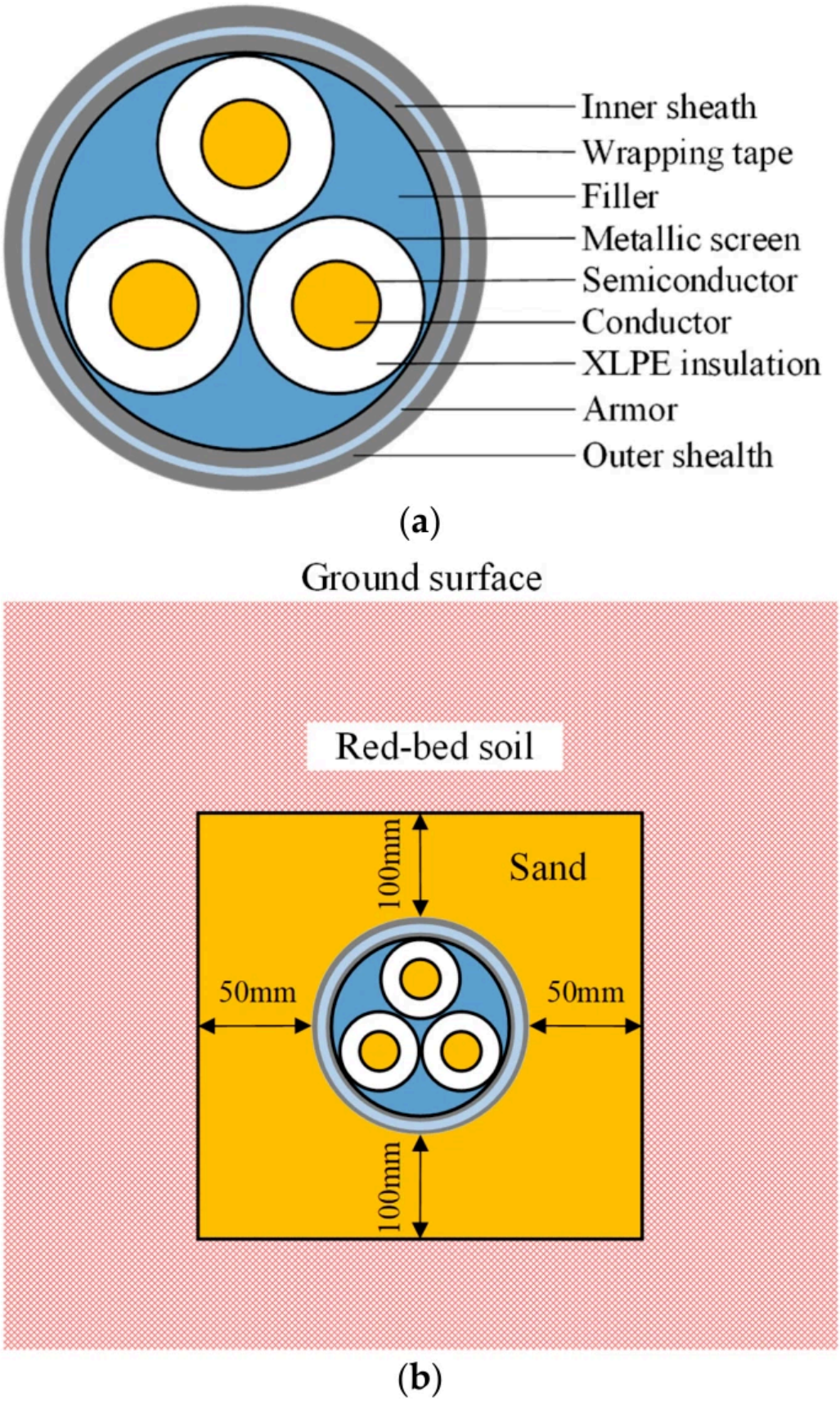


Figure 1. Schematic of YJLV22-26/35 3 × 400 cable structure and installation: (**a**) Schematic of cable structure; (**b**) Schematic of cable installation.

Table 1. Cable structural dimensions and thermal properties.

Material	Thickness (mm)	Diameter (mm)	Thermal Conductivity [W/(m·K)]
Aluminum conductor	-	22.6	217.7
Inner semiconductor	0.8	24.2	0.29
XLPE insulation	10.5	45.2	0.29
Outer semiconductor	1	47.2	0.29
Metallic screen	0.1	47.4	400
Wrapping tape	1.5	105.1	0.2
Inner sheath	1.4	107.9	0.2
Armor	0.8	109.5	49.3
Outer sheath	4.9	119.3	0.2

The cable installation is depicted in Figure 1b. According to construction specifications, fine-sand backfill is required around the cable, with a minimum thickness of 100 mm for the upper and lower layers and a minimum width of 50 mm for the side layers. This paper addresses cable operation scenarios in Southwest China, a region predominantly characterized by red-bed soil. So, red-bed soil is used as backfill outside the fine-sand zone and compacted.

2.2. Soil Thermal Conductivity

Soil thermal conductivity is a key factor governing cable heat dissipation. It depends on saturation S_r, dry density ρ_d, quartz volume fraction q, and porosity n. This study adopts the Johansen model [34] to calculate soil thermal conductivity, as expressed in (1)–(6). Here, λ_{sat} and λ_{dry} denote the thermal conductivities of fully saturated and completely dry soil, respectively, both in W/(K·m). K_e is the Kersten coefficient, with separate formulations for coarse- and fine-grained soils. λ_s is the thermal conductivity of the solid soil phase, which varies with quartz content. λ_q is the thermal conductivity of quartz, taken as 7.7 W/(K·m) [35]. λ_o is the thermal conductivity of other minerals: 3 when $q \le 0.2$, and 2 when $q > 0.2$. ρ_w is the density of water, taken as 1 g/cm^3.

$$\lambda = (\lambda_{sat} - \lambda_{dry})K_e + \lambda_{dry} \tag{1}$$

$$\begin{cases} K_e = 0.7\log S_r + 1, \ \text{Coarse-grained soil} \\ K_e = \log S_r + 1, \ \text{Fine-grained soil} \end{cases} \tag{2}$$

$$\lambda_{dry} = \frac{0.135\rho_d + 64.7}{2700 - 0.947\rho_d} \tag{3}$$

$$\lambda_{sat} = \lambda_w^{\,n} \cdot \lambda_s^{\,1-n} \tag{4}$$

$$\lambda_s = \lambda_q^{\,q} \cdot \lambda_o^{\,1-q} \tag{5}$$

$$n = 1 - \frac{\rho_d}{G_s\rho_w} \tag{6}$$

The dry density and specific gravity of the fine-sand cushion are adopted from [36], with the solid-phase thermal conductivity calculated using (5) and the quartz volume fraction taken as 0.8. The physical properties of red-bed soil follow the values reported in [37] and are summarized in Table 2.

Table 2. Thermal properties of soil around the cable.

Thermal Property	Fine-Sand	Red-Bed Soil
Grain density ρ_s (kg/m^3)	2666	2690
Dry density ρ_d (kg/m^3)	1820	1572
Porosity n	0.32	0.42
Solid thermal conductivity λ_s [W/(K·m)]	5.88	2.69
Quartz volumetric fraction q	0.8	0.22

2.3. Governing Equations of the Thermal Field

The governing equation of the thermal field is given in (7), where T is the temperature field, λ is the soil thermal conductivity [W/(K·m)], and Q is the heat source (W/m^3).

$$\frac{\partial}{\partial x}\left(\lambda\frac{\partial T}{\partial x}\right)+\frac{\partial}{\partial y}\left(\lambda\frac{\partial T}{\partial y}\right)+Q=0 \tag{7}$$

The heat source comprises resistive loss in the conductor P_r, dielectric loss in the insulation P_{XLPE}, copper screen loss P_{co}, and steel tape armor loss P_{armor}. All these loss components are calculated using the methods recommended in IEC 60287 [7]. P_r is computed by (8), where I is the conductor current (A), R_{dc} is the DC resistance of the conductor (Ω/m), R_{ac} is the AC resistance (Ω/m), y_s is the skin effect coefficient, and y_p is the proximity effect coefficient.

$$\begin{cases} P_r = I^2 R_{dc}\left(1+y_s+y_p\right) \\ R_{dc} = \dfrac{\rho\left[1+\alpha_t\left(T_M-20\right)\right]}{A} \end{cases} \tag{8}$$

The skin effect coefficient y_s and proximity effect coefficient y_p are calculated using (9) and (10), where f is the power frequency (set to 50 Hz), s is the center-to-center distance between adjacent phase conductors (m), and d_c is the outer radius of the conductor (m). k_s and k_p are constants determined by cable construction, with $k_s = 1$ and $k_p = 0.8$ [25].

$$\begin{cases} y_s = \dfrac{{x_s}^4}{192+0.8{x_s}^4} \\ {x_s}^2 = \dfrac{8\pi f}{R_{dc}} k_s \times 10^{-7} \end{cases} \tag{9}$$

$$\begin{cases} y_p = \dfrac{{x_p}^4}{192+0.8{x_p}^4}\left(\dfrac{d_c}{s}\right)^2 \times \left[0.312\left(\dfrac{d_c}{s}\right)^2 + \dfrac{1.18}{\dfrac{{x_p}^4}{192+0.8{x_p}^4}+0.27}\right] \\ {x_p}^2 = \dfrac{8\pi f}{R_{dc}} k_p \times 10^{-7} \end{cases} \tag{10}$$

P_{XLPE} is calculated using (11), where ω is the angular frequency (set to 314 rad/s), C is the cable capacitance per unit length (F/m), U_0 is the phase-to-ground voltage (V), and tanδ is the dielectric loss tangent of the insulation material, taken as 0.005 [10]. ε_0 is the vacuum permittivity, 8.85×10^{-12} F/m. ε is the relative permittivity of the XLPE insulation, and D_i is the outer radius of the insulation layer (m).

$$\begin{cases} P_{XLPE} = \omega C U_0^{\,2} tan\delta \\ C = \dfrac{2\pi\varepsilon_0\varepsilon}{\ln\left(D_i/d_c\right)} \end{cases} \tag{11}$$

The copper screen loss is calculated using (12), where λ_1 and λ_2 are the copper screen loss factor and steel tape armor loss factor, respectively. Based on the calculation method in IEC 60287 [7], their values are 0.01 and 0.04, respectively.

$$\begin{cases} P_{co} = \lambda_1 P_r \\ P_{armor} = \lambda_2 P_r \end{cases} \tag{12}$$

2.4. Boundary Conditions

The boundary conditions of the FEM model are illustrated in Figure 2. The left and right lateral boundaries B_1 are treated as insulated, assigned Neumann boundary conditions. The ground surface boundary B_2 incorporates solar irradiance, convection, and radiative heat dissipation, modeled with a mixed boundary condition. The deep-soil boundary B_3 is set as a Dirichlet boundary at a constant temperature of 20 °C. The boundary condition expressions are given in (13), where h_c is the convection coefficient of air, T_s is the ground surface temperature, T_{air} is the ambient temperature, ε_s is the surface emissivity, α is the solar irradiance absorptivity, σ is the Stefan–Boltzmann constant (5.67×10^{-8} W/(m^2·K^4)), and P_{solar} is the solar irradiance in W/m^2.

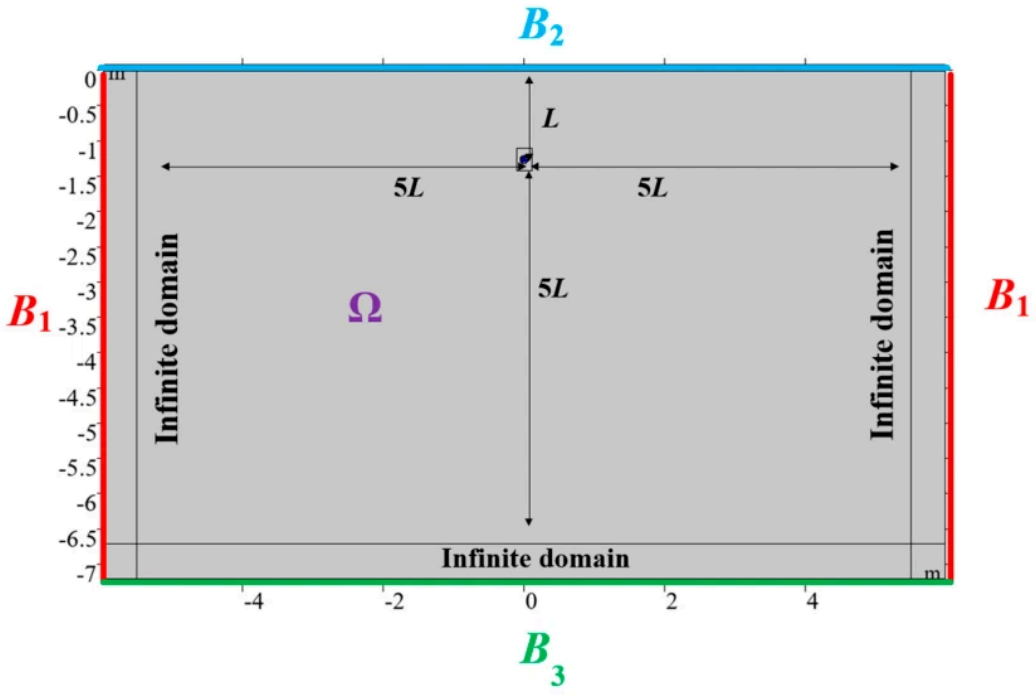
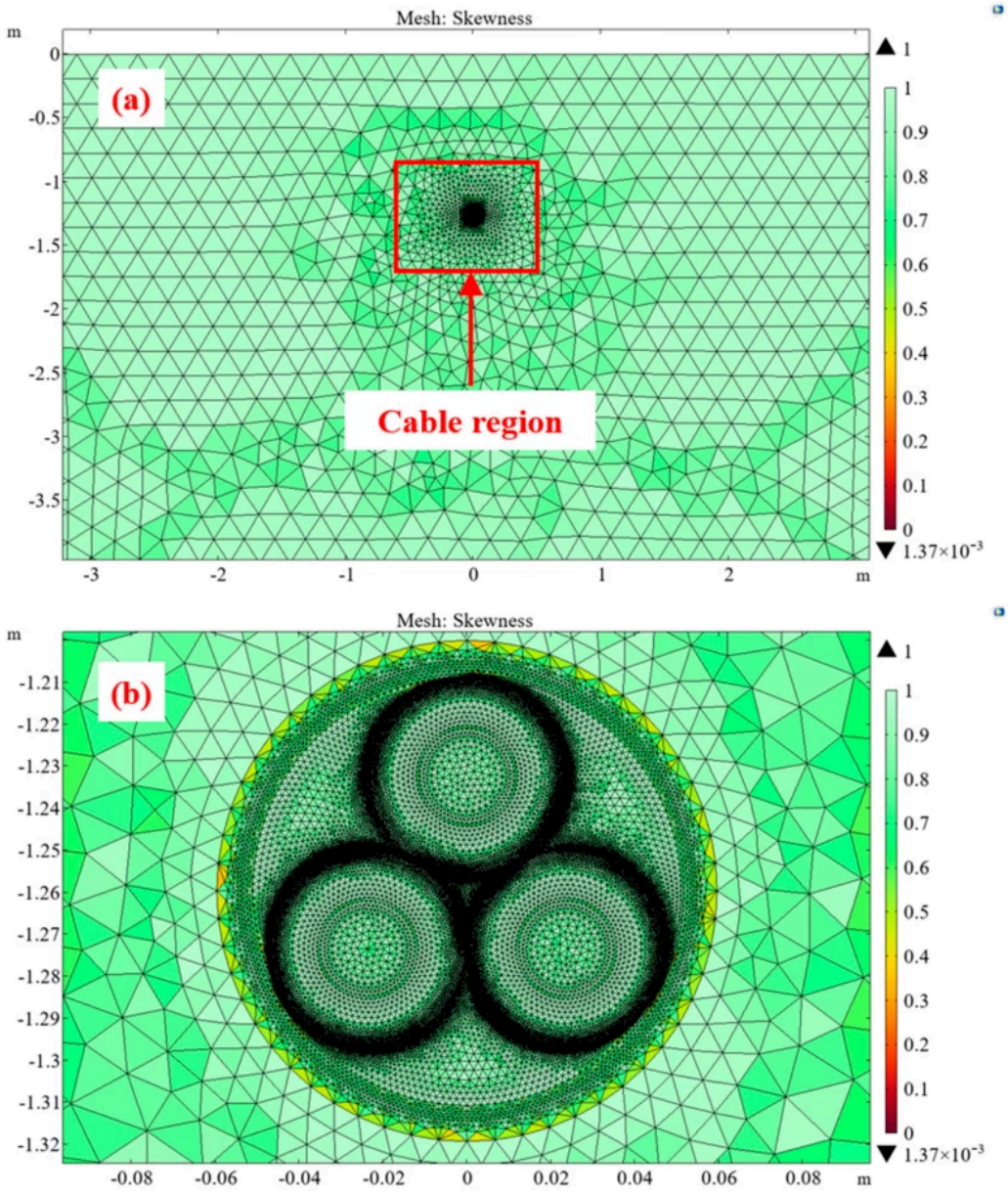


Figure 2. Boundary conditions of the FEM computational model (L = 1.2 m; computational domain 12.0 m × 7.2 m).

The computational domain measures $10L \times 6L$, where L = 1.2 m is the burial depth measured from the ground surface to the cable surface, i.e., 12.0 m × 7.2 m. The lateral and bottom boundaries are positioned at $5L$ from the cable center, and infinite element regions are applied on the left, right and bottom sides of the domain to represent the semi-infinite extent of the soil. All simulations reported in Sections 3 and 4 were performed at this depth; the mesh statistics of Table 4 and the domain views of Figures 2 and 3 correspond to the same 1.2 m model.

$$\begin{cases} B_1 : -\lambda \dfrac{\partial T}{\partial n} = 0 \\ B_2 : -\lambda \dfrac{\partial T}{\partial n} = h_c \left(T_s - T_{air} \right) + \varepsilon_s \sigma \left({T_s}^4 - {T_{air}}^4 \right) - \alpha_{solar} P_{solar} \\ B_3 : T = Const \end{cases} \tag{13}$$



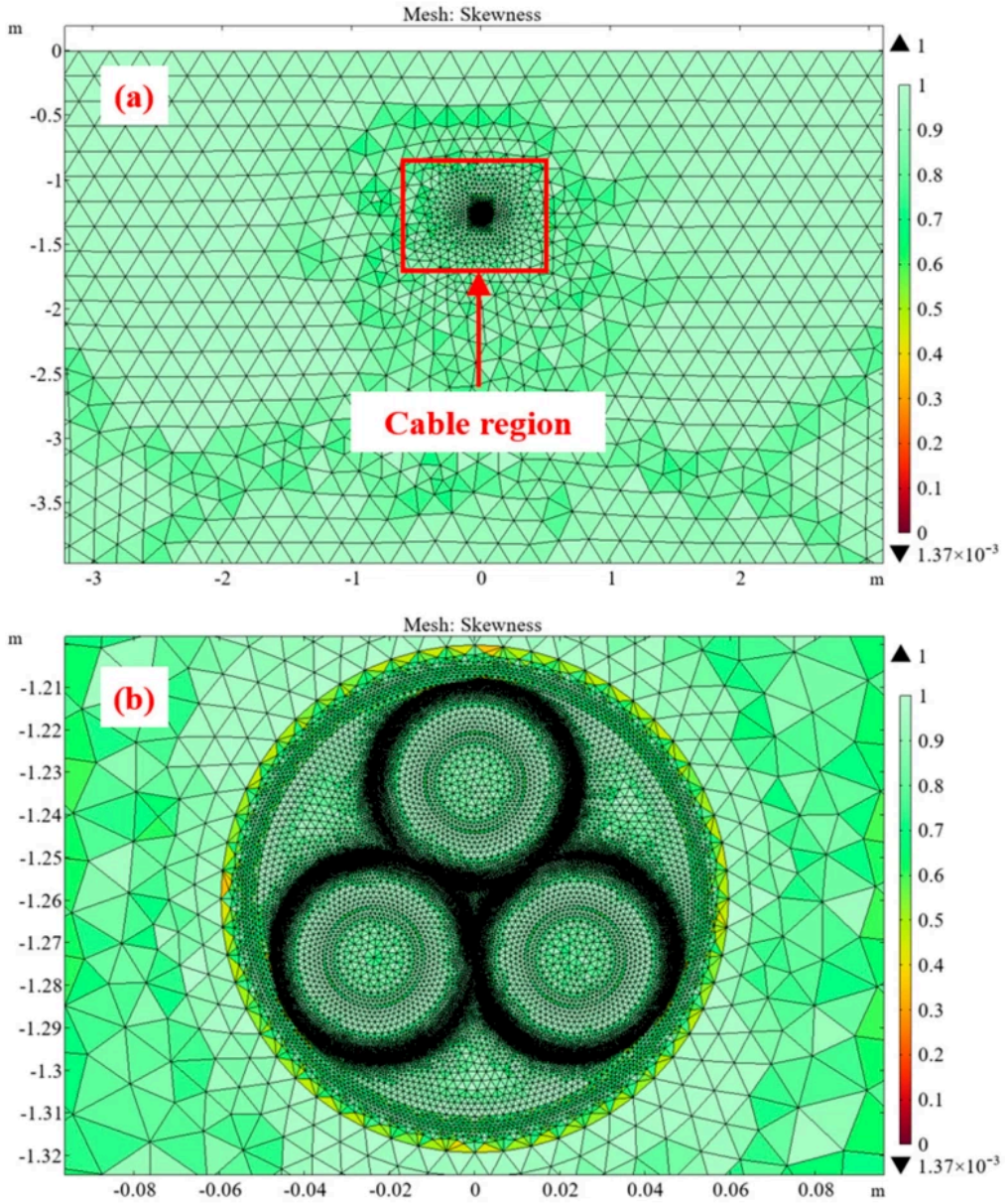


Figure 3. Mesh discretization of the L = 1.2 m model: (**a**) Global view; (**b**) Zoomed-in view.

For the convection coefficient h_c in (13), this study adopts the empirical formula recommended in [32], expressed as (14), where v is the wind speed (m/s). This model adopts a light-breeze wind speed (v = 2.5 m/s), applicable to most typical scenarios.

$$h_c = 11.4 + 5.7v \quad (14)$$

The environmental parameters used in this model are summarized in Table 3.

Table 3. Environmental parameters adopted in this study.

Environmental Parameters	Value	Unit
Soil thermal conductivity λ	Equation (1)	W/(K·m)
Ambient temperature T_{air}	25	°C
Solar irradiance P_{solar}	1000	W/m^2
Solar absorptivity α_{solar}	0.6	-
Surface emissivity ε_s	0.94	-

Environmental Parameters	Value	Unit
Convection coefficient h_c	Equation (14)	W/(m^2·K)
Wind speed v	2.5	m/s
Cable burial depth L	1.2	m

2.5. Mesh Generation

The computational domain was discretized using physics-controlled adaptive mesh refinement, with the extra fine mesh option provided by COMSOL Multiphysics 6.2. A locally dense mesh was implemented at the cable surface, while relatively coarse yet uniform elements were employed in the remaining regions, as illustrated in Figure 3. The mesh statistics are presented in Table 4. The mesh employs triangular elements, comprising a total of 344,062 cells with an average element quality of 0.8642, indicating excellent mesh quality. The domain and the mesh views refer to L = 1.2 m (12.0 m × 7.2 m).

Table 4. Statistics of mesh discretization.

Mesh Parameter	Value
Number of triangles	344,062
Number of edge elements	16,904
Number of vertex elements	98
Minimum element quality	0.001374
Average element quality	0.8642
Element area ratio	3.626×10^{-12}
Mesh area	86.4 m^2

2.6. Model Consistency and Comparison with IEC 60287

To establish the physical reliability of the proposed electro-thermal-fluid multiphysics FEM model, a systematic consistency check was performed against the analytical standard IEC 60287 under identical homogeneous-soil and constant-surface-temperature conditions. This section verifies that the FEM solver accurately reproduces the steady-state heat conduction process, while the residual discrepancies are attributed to inherent model simplifications rather than numerical errors.

2.6.1. Thermal Resistance Decomposition

The total thermal resistance was decomposed into its constituent layers: XLPE insulation, inner sheath, outer sheath, and external soil. As illustrated in Figure 4a, the FEM-derived equivalent thermal resistances show close agreement with IEC 60287 calculations across all components. Specifically, the soil external thermal resistance dominates the total resistance, with both methods yielding an identical value of 2.9 K·m/W. For the internal cable layers, FEM predicts slightly higher values (XLPE: 0.8 vs. 0.6 K·m/W; inner sheath: 0.5 vs. 0.3 K·m/W; outer sheath: 0.4 vs. 0.3 K·m/W), reflecting the distributed-field nature of the FEM model compared to the lumped-parameter approximation of IEC 60287. The overall summation remains highly consistent, confirming that the thermal circuit representation in the FEM framework aligns with the standard analytical approach.

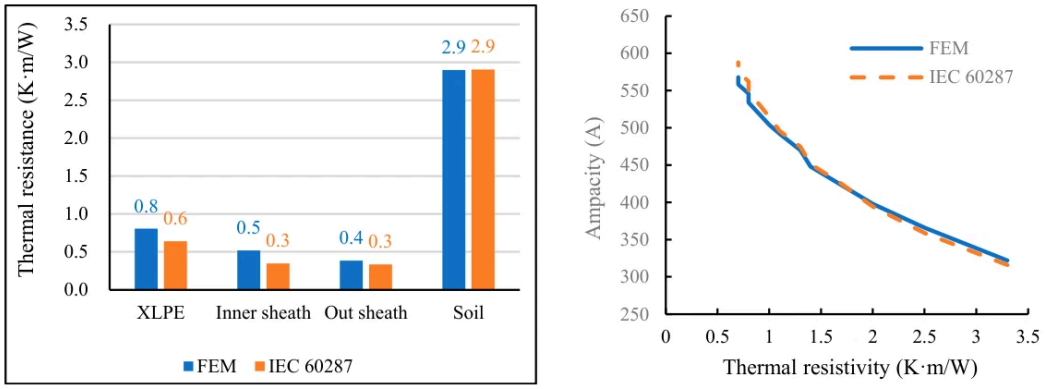


Figure 4. Comparison of thermal resistance and ampacity from FEM and IEC 60287 analytical method (Surface temperature T_g = 25 °C, conductor temperature T = 90 °C). (**a**) Thermal resistance; (**b**) Ampacity.

2.6.2. Ampacity Trend and Solver Verification

Building on the thermal resistance agreement, the ampacity variation with soil thermal resistivity was evaluated, as shown in Figure 4b. The FEM and IEC 60287 curves exhibit a strictly monotonic decreasing trend with increasing thermal resistivity, maintaining close visual overlap with an average deviation below 3.4% across the 0.7–3.3 K·m/W range. This high degree of concordance provides a numerical verification of the FEM solver for the steady-state heat conduction equation.

2.6.3. Physical Consistency and Transition to Real-World Scenarios

The combined evidence from thermal resistance decomposition and ampacity trends confirms that both models describe the same underlying heat dissipation mechanism. Under the simplified homogeneous baseline, the FEM model is numerically verified against IEC 60287. This verified baseline subsequently supports the extension to real-world direct-buried conditions, where layered red-bed/sand backfill, spatially varying saturation, and diurnal solar irradiance introduce complexities beyond the analytical standard's scope. The current evaluation remains steady-state; transient thermal processes under sudden load or meteorological changes are acknowledged as a limitation and reserved for future multiphysics extension.

2.7. Limitations of the Model

The proposed FEM model offers improved fidelity over IEC 60287 for steady-state ampacity evaluation of directly buried cables; however, several limitations should be noted.

(1) The moisture field is not solved interactively. Saturation is prescribed as a spatial input rather than evolved as a state variable. Moisture transport, evaporation, and soil-drying kinetics are not simulated; the model therefore predicts the thermal consequence of a given saturation distribution, not its time evolution.

(2) Two-dimensional geometry and circuit simplification. The analysis is confined to a 2D cross-section, excluding joints, terminations, and axial variation in the backfill. Only a single circuit carrying a balanced three-phase load is considered; grouping effects from multiple circuits, harmonic losses, and load imbalance are not represented.

(3) Material parameters from literature with bounded applicability. Soil thermal conductivity follows the Johansen model with parameters taken from published data

rather than site-specific measurements. For the fine-grained branch, the Kersten coefficient becomes negative below S_r = 0.1, restricting the red-bed soil to S_r > 0.1 throughout. Cable material properties (XLPE, sheath) are treated as temperature-independent within the steady-state loop, whereas in practice dielectric loss and resistivity exhibit thermal coupling.

(4) No experimental validation. Verification to date is strictly model-to-model: the agreement with IEC 60287 in Section 2.6, comprising the thermal-resistance decomposition, the ampacity-trend comparison and the solver check, is a numerical benchmark, not experimental confirmation.

(5) Surface boundary simplification and steady-state assumption. The surface boundary employs a clear-sky sinusoidal model with constant wind speed. Cloud cover, shading, vegetation, rainfall, seasonal variation, and freezing are omitted. The quasi-steady treatment of the diurnal cycle neglects backfill thermal inertia: the daytime peak derating is conservative, whereas the night-time 100% ratios are artifacts of the zero-irradiance steady-state boundary and do not represent the actual cable condition. Hour-by-hour operating schedules, dynamic rating and emergency-overload prediction would require a transient model that resolves soil heat capacity and the daily thermal history; such a calculation is not presented here. The entire evaluation is steady-state.

3. Results and Analysis

3.1. Influence of Saturation

Figure 5 shows the variation of thermal conductivity with saturation for fine-sand and red-bed soil, calculated from the Johansen model expressed as (1). Both clearly exhibit a nonlinear, monotonically increasing trend. In the low-saturation range (S_r < 0.3), thermal conductivity rises sharply with increasing saturation, after which the growth rate gradually diminishes. The underlying reason is that at low saturation, pore spaces are filled with air; as saturation rises, water displaces air, and water's thermal conductivity is substantially higher than that of air.

Figure 6 shows the dependence of ampacity on saturation degree. Both the IEC 60287 analytical method and the FEM indicate that ampacity increases nonlinearly with saturation degree. For instance, for a layered soil backfill structure, when the saturation degree increases from 0.1 to 0.3, the ampacity increases by 58.5%, by 11.5% from 0.3 to 0.6, and by only 5.5% from 0.6 to 1.0. In addition, the figure compares the ampacity variation ranges with saturation degree obtained from the IEC 60287 analytical method and FEM without considering surface convection and solar irradiance, for the cases of all-fine-sand and all-red-clay soil. It can be seen that the calculated values based on the IEC analytical method are higher than those from FEM. For the all-fine-sand case, the current error ranges from 3.97% to 7.34%. For the all-red-clay case, the current error ranges from 0.61% to 4.88%.

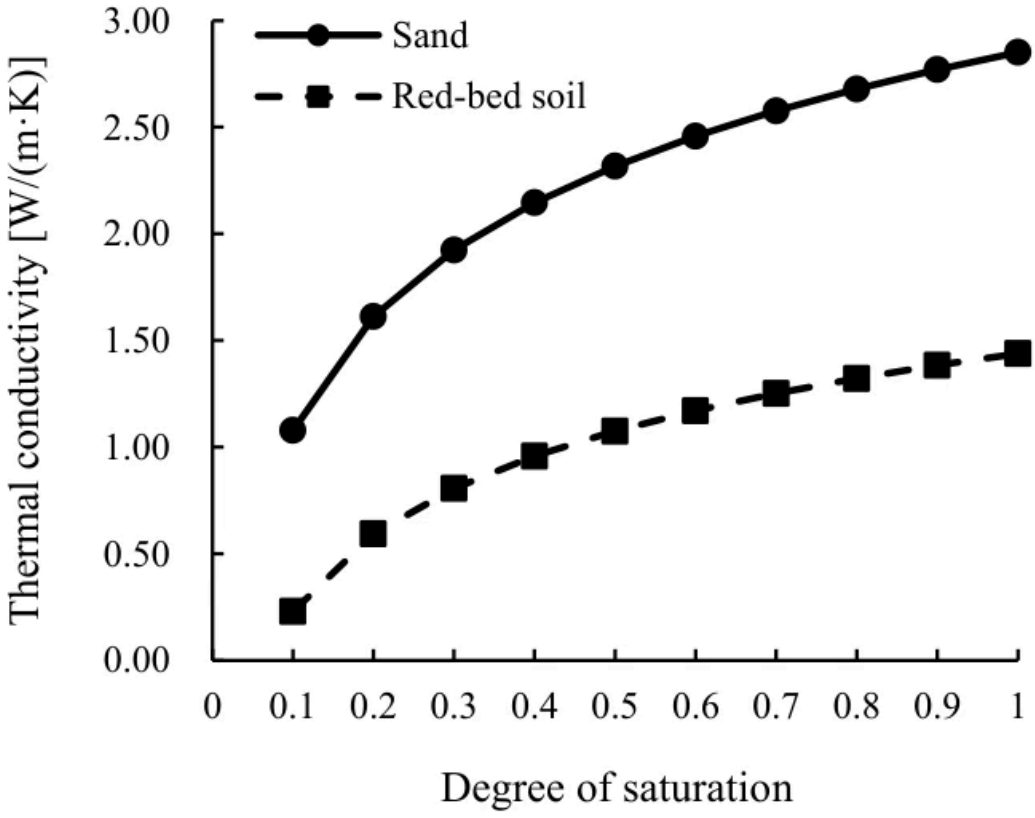


Figure 5. Thermal conductivity of fine sand and red-bed soil versus degree of saturation (Johansen model).

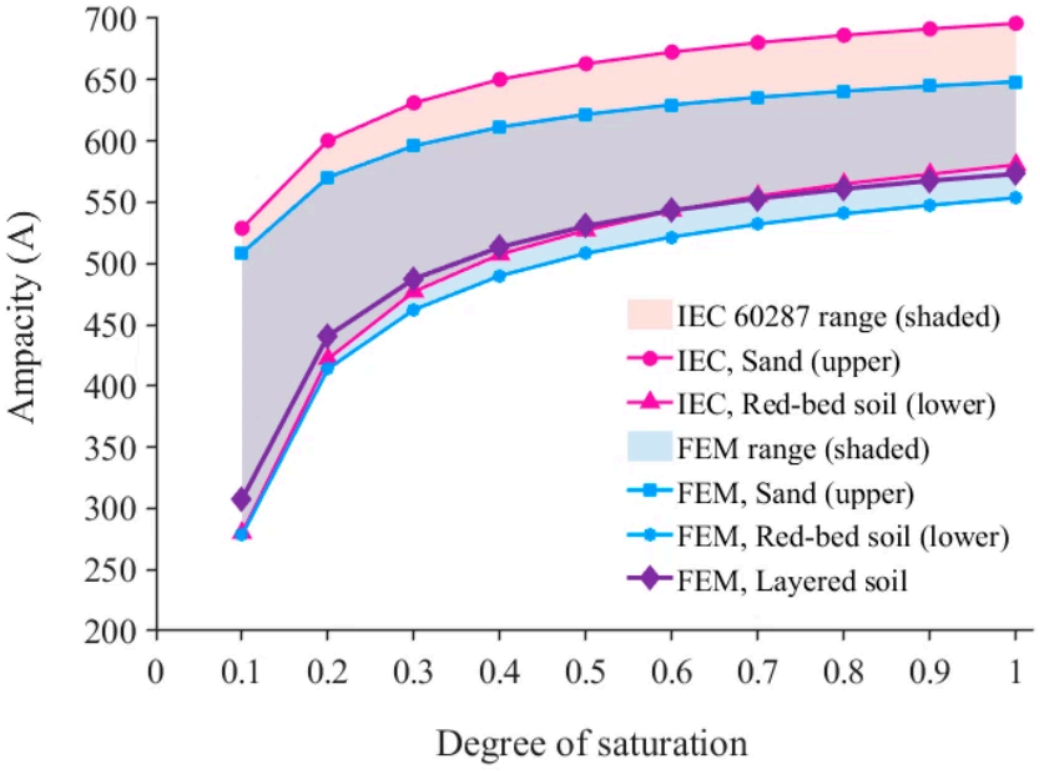


Figure 6. Influence of saturation on the ampacity (Surface temperature T_g = 25 °C, conductor temperature T = 90 °C, without accounting for surface convection, solar irradiance, and surface thermal radiation).

This systematic overestimation by IEC stems from its simplified one-dimensional equivalent thermal circuit, which yields lower internal layer resistances (as seen in Figure 4a) compared to the multi-dimensional heat-flow solution captured by FEM. Since the soil thermal resistance is nearly identical between the two methods (2.9 K·m/W), the discrepancy is dominated by the underestimated cable-internal thermal resistance in IEC. This effect is more pronounced in fine sand, where the lower soil thermal resistance amplifies the relative contribution of internal layer resistance, leading to larger current deviations; in red-bed soil, the higher soil resistance dominates and masks the internal discrepancy, resulting in smaller differences. Additionally, the FEM result for layered backfill soil falls between the upper (fine sand) and lower (red-bed soil) boundary curves, confirming that the layered configuration yields an intermediate ampacity response within the range defined by the two homogeneous soils.

3.2. Influence of Fine-Sand Backfill Thickness

The thermal conductivity of fine-sand is more than twice that of red-bed soil; increasing the fine-sand backfill thickness therefore enhances cable heat dissipation. Based on the condition of P_{solar} = 1000 W/m^2 and v = 2.5 m/s, the effect of fine-sand backfill thickness above the cable on ampacity is shown in Figure 7. Ampacity increases nonlinearly with backfill thickness. When the thickness increases from 0.1 m to 0.7 m, ampacity rises by 17 A (6.5%) at S_r = 0.1 and by 10 A (2.7%) at S_r = 0.2. For S_r > 0.3, the increase is less than 9 A, with a gain below 2.2%. This indicates that the benefit of adding fine-sand backfill thickness is saturation-dependent: it effectively boosts ampacity only under dry soil conditions, whereas additional sand thickness yields negligible improvement in moist soils.

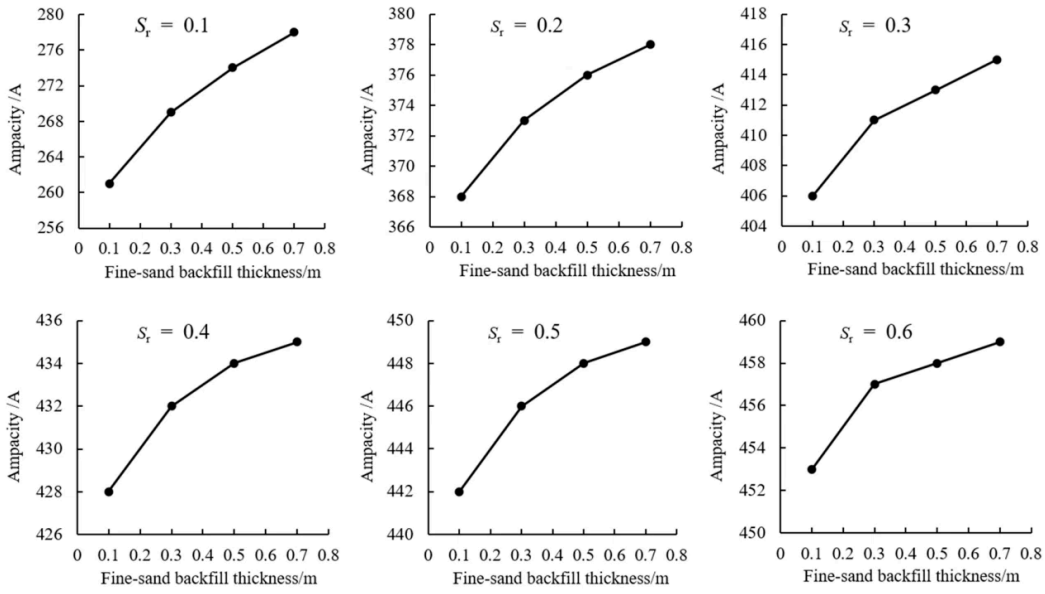


Figure 7. Influence of fine-sand cushion thickness on ampacity (P_{solar} = 1000 W/m^2, v = 2.5 m/s, T = 90 °C).

3.3. Influence of Solar Irradiance Variation

Solar irradiance elevates soil temperature, thereby reducing cable ampacity. To obtain the solar irradiance variation curves, this study downloaded solar irradiance data for the Dali region in China from the NASA POWER Data Access Viewer (DAV) [38]. Figure 8 presents the diurnal variation curves of solar irradiance in January and July. As can be seen, the diurnal variation curve of solar irradiance approximates a sinusoidal

profile; therefore, a sinusoidal curve is adopted in this paper to simulate the solar irradiance variation. According to IEC 60287-3-1 [11], the solar irradiance for regions in China may be taken as 1000 W/m^2 [11]. Regarding the surface solar irradiance absorptivity, this study refers to IEC 60287-1-1 [11,39] and assigns a value of 0.6, while the surface emissivity is taken as 0.94.

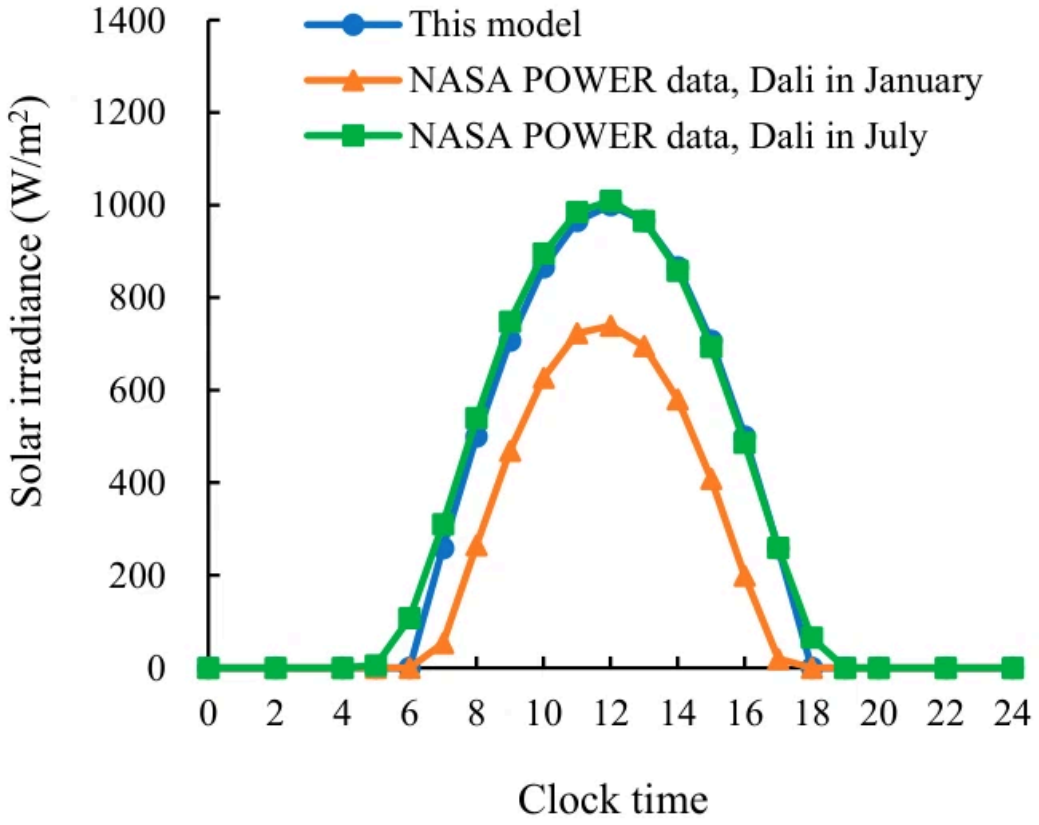
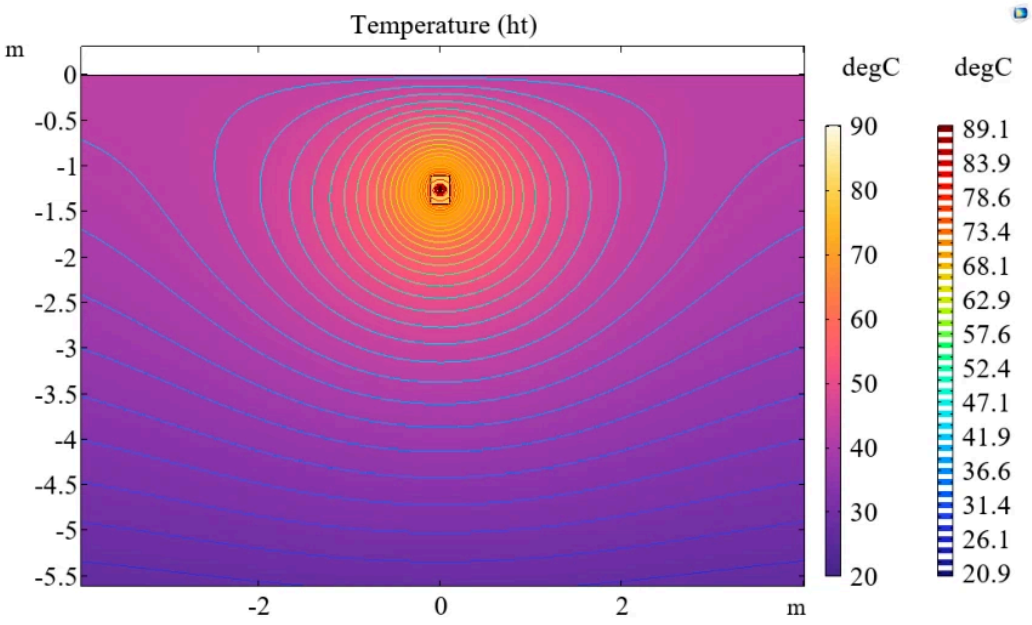
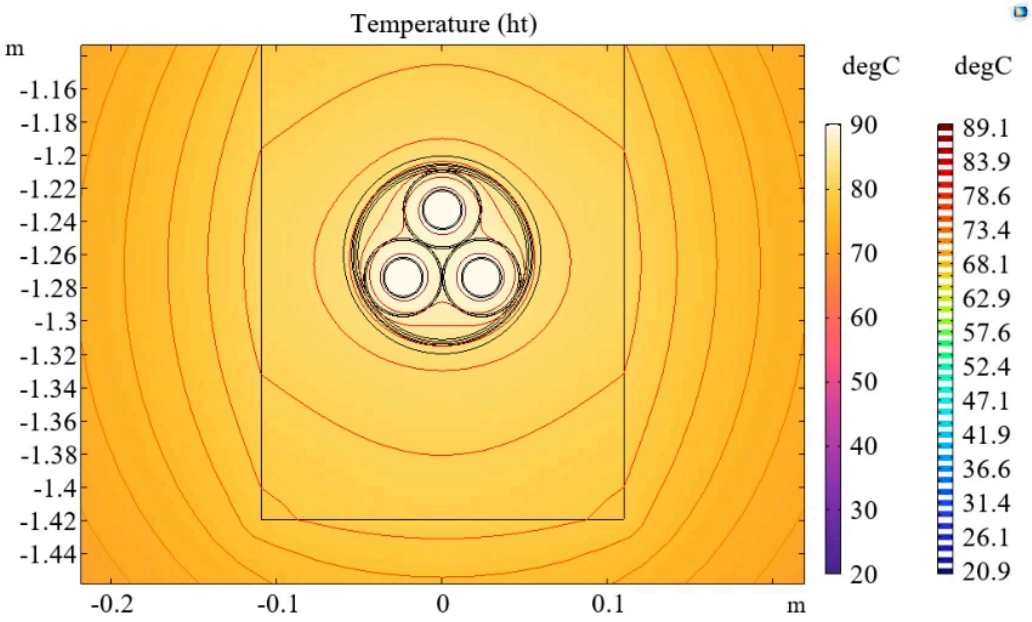


Figure 8. Diurnal variation of solar irradiance with time.

Under a solar irradiance of P_{solar} = 1000 W/m^2, wind speed v = 2.5 m/s, degree of saturation S_r = 0.3, and conductor current I = 369 A, the cable conductor temperature reaches 90 °C, and the resulting temperature field distribution is presented in Figure 9. The global view reveals a pronounced concentric thermal gradient centered at the buried three-core cable, with temperatures decaying radially from the hot conductor core (~90 °C) outward through the backfill and into the surrounding soil, eventually approaching the far-field temperature of 20–25 °C at depth and lateral distance. The magnified local view resolves the individual conductors and their immediate insulation layers, confirming that the 90 °C isotherm is confined strictly to the conductor region while the backfill and adjacent soil remain at substantially lower temperatures, with clear isotherm spacing indicating effective radial heat dissipation.


Temperature (ht)
m
0
-0.5
-1
-1.5
-2
-2.5
-3
-3.5
-4
-4.5
-5
-5.5
-2
0
2
m
degC
90
80
70
60
50
40
30
20
degC
89.1
83.9
78.6
73.4
68.1
62.9
57.6
52.4
47.1
41.9
36.6
31.4
26.1
20.9

(a)


Temperature (ht)
m
-1.16
-1.18
-1.2
-1.22
-1.24
-1.26
-1.28
-1.3
-1.32
-1.34
-1.36
-1.38
-1.4
-1.42
-1.44
-0.2
-0.1
0
0.1
m
degC
90
80
70
60
50
40
30
20
degC
89.1
83.9
78.6
73.4
68.1
62.9
57.6
52.4
47.1
41.9
36.6
31.4
26.1
20.9

(b)

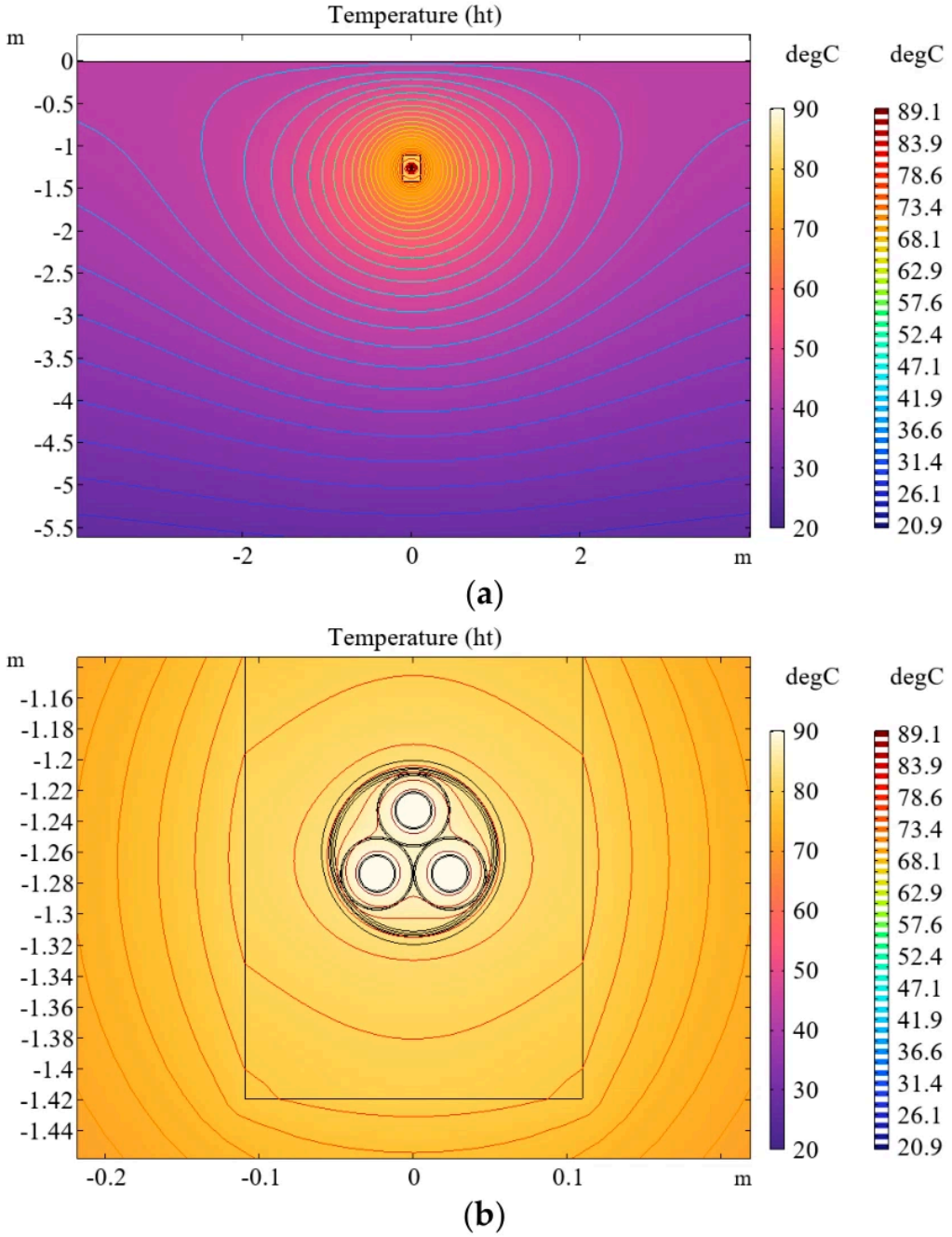


Figure 9. Distribution of the cable temperature field: (**a**) global view; (**b**) magnified local view (P_{solar} = 1000 W/m^2, v = 2.5 m/s, S_r = 0.3, I = 369 A).

The ampacity of the cable exhibits a strong dependence on both solar irradiance and saturation, as illustrated in Figure 10. It can be observed that, at a given saturation level, increasing solar irradiance from 0 to the maximum of 1000 W/m^2 reduces the cable ampacity by approximately 20%. The minimum ampacity of 260 A occurs under the combined conditions of the lowest saturation (S_r = 0.1) and the highest solar irradiance (P_{solar} = 1000 W/m^2). Conversely, the maximum ampacity of 604 A is achieved at full saturation (S_r = 1) with zero solar irradiance. Therefore, for cable circuits where substantial variations in soil saturation may be encountered along the route, the rated ampacity should be determined based on the section with the lowest saturation level at solar noon.

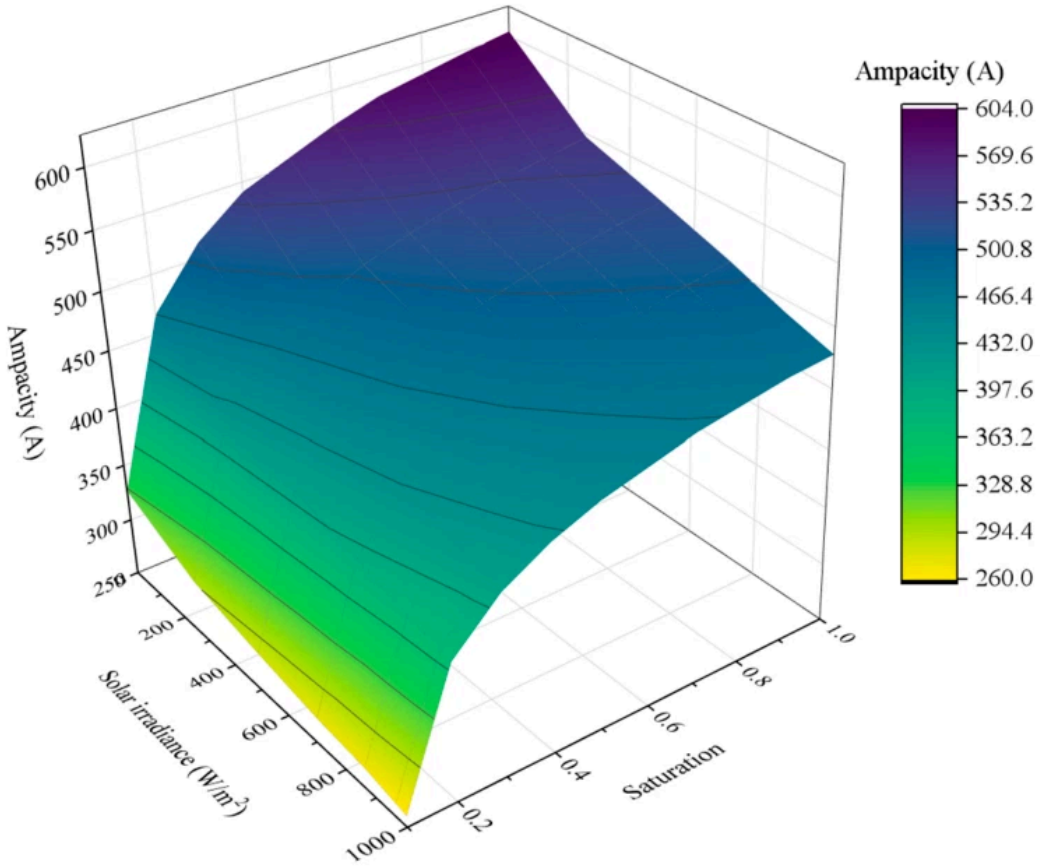


Figure 10. Dependence of cable ampacity on solar irradiance and saturation.

Based on the diurnal solar irradiance profile, the cable ampacity at different times of day can be obtained, as shown in Figure 11. Under varying saturation levels, solar irradiance exerts a consistent influence on ampacity across all cases, following a half-wave cosine variation. The minimum ampacity occurs at solar noon.

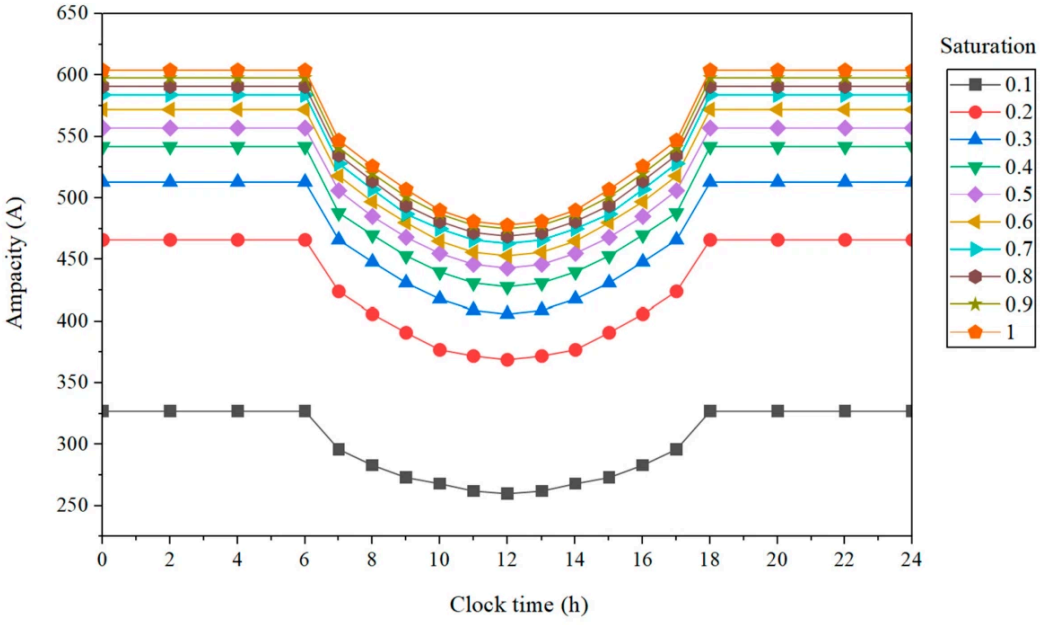


Figure 11. Diurnal variation of cable ampacity with solar irradiance.

The curves of Figures 9–11 were obtained by solving the steady-state problem sepa-

rately for each value of the irradiance, that is, by treating the instantaneous irradiance as if it were sustained. The thermal inertia of the backfill modifies this picture, and the question is examined in Section 3.5.

3.4. Influence of Spatial Saturation Distribution

To examine the coupling effect of spatially distributed saturation between fine-sand and red-bed soil on ampacity, seven cases were established. Case 1: both sand and red-bed soil are fully saturated; Case 2: saturation degree is 0.8 for both, representing wet conditions. Case 3: saturation degree is 0.3 for both, representing moderate saturation. Case 4: dry sand with wet red-bed soil. Case 5: wet sand with dry red-bed soil. Case 6: saturation degree is 0.1 for both, representing dry conditions. Case 7: completely dry. The thermophysical properties for each case are given in Table 5. To distinguish the saturation and thermal conductivity of different soil layers, S_{r_sand} and S_{r_red} denote the saturation of fine-sand and red-bed soil, respectively, while λ_{sand} and λ_{red} denote their respective thermal conductivities.

Table 5. Soil Thermophysical Properties for the Seven Operation Scenarios.

Operation Scenarios	Saturation	Thermal Conductivity (W/(m·K))	Remarks
Case 1	$S_{r_sand} = 1$ $S_{r_red} = 1$	$\lambda_{sand} = 2.84$ $\lambda_{red} = 1.44$	Fully saturation
Case 2	$S_{r_sand} = 0.8$ $S_{r_red} = 0.8$	$\lambda_{sand} = 2.68$ $\lambda_{red} = 1.32$	Wet
Case 3	$S_{r_sand} = 0.3$ $S_{r_red} = 0.3$	$\lambda_{sand} = 1.92$ $\lambda_{red} = 0.81$	Moderate saturation
Case 4	$S_{r_sand} = 0.3$ $S_{r_red} = 0.8$	$\lambda_{sand} = 1.92$ $\lambda_{red} = 1.32$	Dry sand with wet soil
Case 5	$S_{r_sand} = 0.8$ $S_{r_red} = 0.3$	$\lambda_{sand} = 2.68$ $\lambda_{red} = 0.81$	Wet sand with dry soil
Case 6	$S_{r_sand} = 0.1$ $S_{r_red} = 0.1$	$\lambda_{sand} = 1.07$ $\lambda_{red} = 0.23$	Dry
Case 7	$S_{r_sand} = 0.05$ $S_{r_red} = 0.1$	$\lambda_{sand} = 0.54$ $\lambda_{red} = 0.23$	Completely dry

Figure 12 shows the variation of ampacity with solar irradiance under the seven operating scenarios. The results indicate that Case 1 (fully saturated) yields the maximum ampacity, forming the upper bound. Case 7 (completely dry) yields the minimum ampacity, forming the lower bound. The ampacities of all other scenarios fall between these two bounds. Cases 2 and 4 both feature wet red-bed soil and exhibit close ampacity values, indicating that sand saturation has a negligible effect on ampacity. Cases 3 and 5 both feature dry red-bed soil, where sand saturation exerts a slight influence on ampacity. Case 6 (both sand and red-bed soil dry) yields an ampacity slightly higher than that of the completely dry condition. From the ampacity distribution, it is evident that sand saturation has minimal impact on ampacity, while red-bed soil saturation dominates the ampacity.

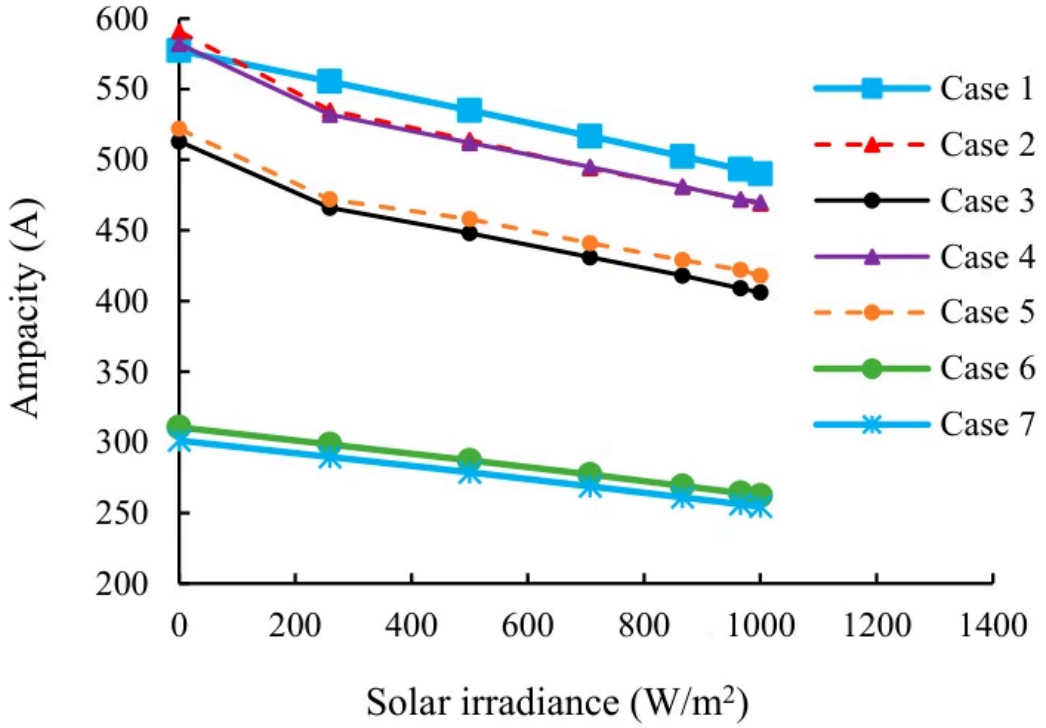


Figure 12. Ampacity comparison among seven operating scenarios with solar irradiance.

3.5. Thermal Inertia and the Quasi-Steady Treatment

The impact of solar irradiance on cable ampacity was evaluated using a quasi-static thermal model, in which the steady-state heat conduction equation is solved at each hourly time step with time-varying surface boundary conditions (solar irradiance, convection, and longwave radiation). This approach does not explicitly resolve soil thermal inertia; however, the physical effect of thermal inertia can be quantified analytically and defines the range of validity of the present method.

The periodic temperature fluctuation equations are given by (15)–(17), where T_m is the mean surface temperature (°C), A is the amplitude of the surface temperature fluctuation (°C), z is the earth depth (m), ω is the angular frequency (rad/s),d is the damping depth (m), λ is the thermal conductivity (W/(K·m)), α is the thermal diffusivity, and ρ_c is the volumetric heat capacity (J/(m^3·K)).

$$T(z,t) = T_m + A \cdot \exp\left(-\frac{z}{d}\right) \cdot \sin\left(\omega t - \frac{z}{d}\right) \tag{15}$$

$$d = \sqrt{\frac{2\alpha}{\omega}} \tag{16}$$

$$\alpha = \frac{\lambda}{\rho_c} \tag{17}$$

With a typical soil thermal resistivity of 1 W/(K·m) and a volumetric heat capacity of 2.0×10^6 J/(m^3·K), the damping depth is calculated to be d = 0.12 m. Therefore, at the burial depth of 1.2 m, the diurnal harmonic is attenuated by a factor of exp(−10), i.e., <0.005% of the surface amplitude. The phase delay exceeds one full diurnal cycle at z > 0.75 m. Consequently, the cable conductor experiences only the daily-mean component of solar heating as a slow, quasi-steady shift in baseline temperature, while the intra-day

fluctuation is effectively filtered by soil thermal inertia.

The quasi-static model, by solving a steady-state problem at each instantaneous irradiance value, implicitly assumes zero thermal inertia and therefore yields the conductor temperature that would result if each hourly solar intensity were maintained indefinitely. For the daytime hours this represents an upper bound of the true intra-day temperature excursion and thus a conservative estimate of the peak solar-induced derating; the converse holds for the night-time hours, as discussed below. For the irradiance profile of Figure 8 (peak 1000 W/m^2, daily mean ≈ 330 W/m^2), the quasi-static approach overestimates the peak cable temperature increment by no more than ~15% of the diurnal swing amplitude—well within engineering safety margins.

In summary, the quasi-static treatment gives a conservative upper bound on the daytime peak temperature rise and hence on the peak solar-induced derating, but it is not conservative for the permissible current at every hour. With zero irradiance imposed at night, the steady-state solution returns an unrestricted 100% ampacity; as shown above, the cable at 1.2 m responds to the daily-mean irradiance, which persists after sunset, so this night-time value is a consequence of the method rather than of the actual cable condition. The hourly ratios in Table 6 should therefore be read as a parametric sensitivity to irradiance, or as a peak-derating envelope, and not as an hour-by-hour operating schedule. A transient formulation that resolves soil heat capacity and the daily thermal history is required for dynamic rating or dispatch decisions; this is stated as a limitation in Section 2.7.

Table 6. Quasi-steady hourly ampacity ratio under varying red-bed soil saturation (parametric values; not an operating schedule).

Clock Time	Cable Ampacity Ratio/%			
	S_r = 0.1	S_r = 0.2	S_r = 0.3	S_r = 0.4
0	100.0	100.0	100.0	100.0
2	100.0	100.0	100.0	100.0
4	100.0	100.0	100.0	100.0
6	100.0	100.0	100.0	100.0
7	90.5	91.0	90.8	90.0
8	86.5	87.1	87.3	86.7
9	83.5	83.9	84.0	83.6
10	82.0	80.9	81.5	81.2
11	80.1	79.8	79.7	79.5
12	79.5	79.2	79.1	79.0
13	80.1	79.8	79.7	79.5
14	82.0	80.9	81.5	81.2
15	83.5	83.9	84.0	83.6
16	86.5	87.1	87.3	86.7
17	90.5	91.0	90.8	90.0
18	100.0	100.0	100.0	100.0
20	100.0	100.0	100.0	100.0
22	100.0	100.0	100.0	100.0
24	100.0	100.0	100.0	100.0

4. Cable Operation Strategy

Building on the simulation results above, this section proposes cable operation con-

trol strategies from three perspectives: saturation regulation, backfill structure optimization, and dynamic ampacity control, thereby providing engineering guidance for the safe operation of directly buried cables.

4.1. Saturation Control of Red-Bed Soil

Figure 12 shows that ampacity under wet red-bed soil conditions (Cases 2 and 4) is on average approximately 15% higher than under dry red-bed conditions (Cases 3 and 5). Therefore, controlling the saturation of red-bed soil is a key strategy for regulating cable ampacity. As shown in Figure 13, which plots the rate of change of soil thermal conductivity, when $S_{r\text{-}red} < 0.3$ the rate exceeds 2, placing thermal resistance in a high-sensitivity zone where small saturation variations cause drastic resistance changes. For $0.3 < S_{r\text{-}red} < 0.6$, the rate falls between 1 and 2, corresponding to a moderate-sensitivity zone. When $S_{r\text{-}red} \geq 0.6$, the rate drops below 1, indicating a low-sensitivity zone where saturation variations have minimal impact on thermal resistance.

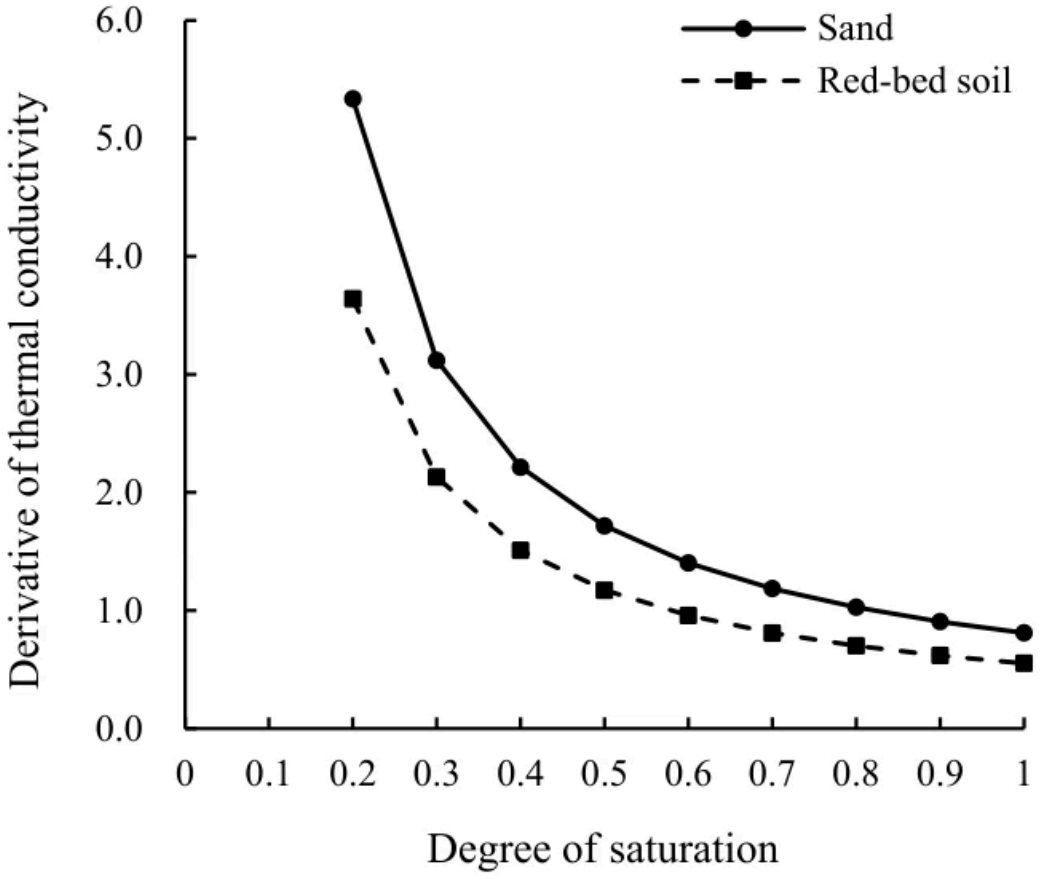
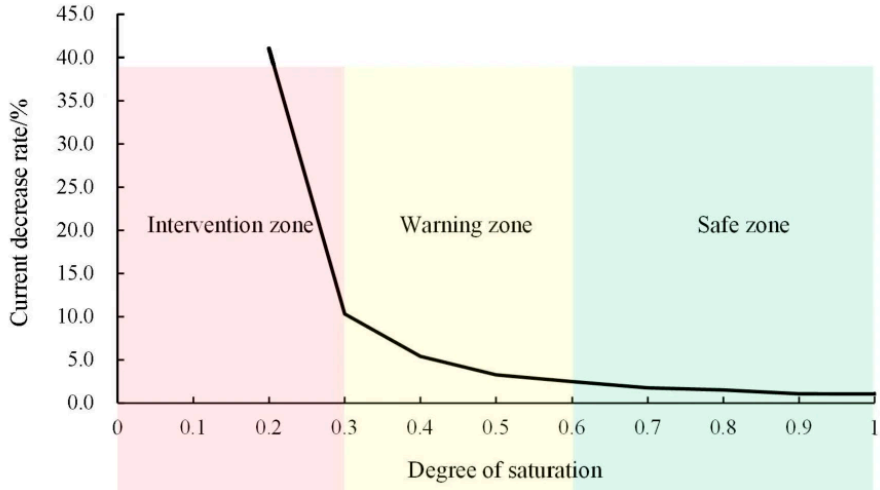


Figure 13. Derivative of the soil thermal conductivity with respect to saturation.

Based on the above analysis, $S_{r\text{-}red} \geq 0.6$ is designated as the safe operating zone, $0.3 \leq S_{r\text{-}red} < 0.6$ as the early-warning zone, and $S_{r\text{-}red} < 0.3$ as the emergency-intervention zone, as illustrated in Figure 14. During cable operation, a soil moisture sensor can be embedded at a depth of 0.3 m above the cable for real-time monitoring, or the moisture content of the shallow (0–0.3 m) and deep (0.6–1.2 m) soil layers can be measured on a weekly basis.



Zone	Intervention zone	Warning zone	Safe zone
Saturation	$S_{r\text{-}red} < 0.3$	$0.3 \leq S_{r\text{-}red} < 0.6$	$S_{r\text{-}red} \geqslant 0.6$
Thermal conductivity (W/(m·K))	$\lambda_{red} < 0.81$	$0.81 < \lambda_{red} < 1.17$	$\lambda_{red} \geqslant 1.17$
Ampacity change rate (%)	$\Delta I > 10.3$	$2.5 \leq \Delta I < 10.3$	$\Delta I \leq 2.5$
Operational recommendation	Water replenishment or ampacity derating	Enhanced monitoring or inspection	Normal monitoring

Figure 14. Saturation control strategy for red-bed soil.

4.2. Optimization of Fine-Sand Cushion Thickness

Figure 15 shows the ampacity increase rate as fine-sand cushion thickness rises from 0.1 m to 0.7 m at different saturations. At S_{r_sand} = 0.1, the increase is 6.51%; at S_{r_sand} = 0.3, it drops to 2.22%; and for $S_{r_sand} \geq 0.4$, the rate remains below 1.64%. Therefore, in arid regions, increasing the fine-sand cushion thickness or replacing it with a high-thermal-conductivity material can effectively boost ampacity. In contrast, humid regions should not rely excessively on cushion thickness; instead, priority should be given to managing the moisture content of the red-bed soil.

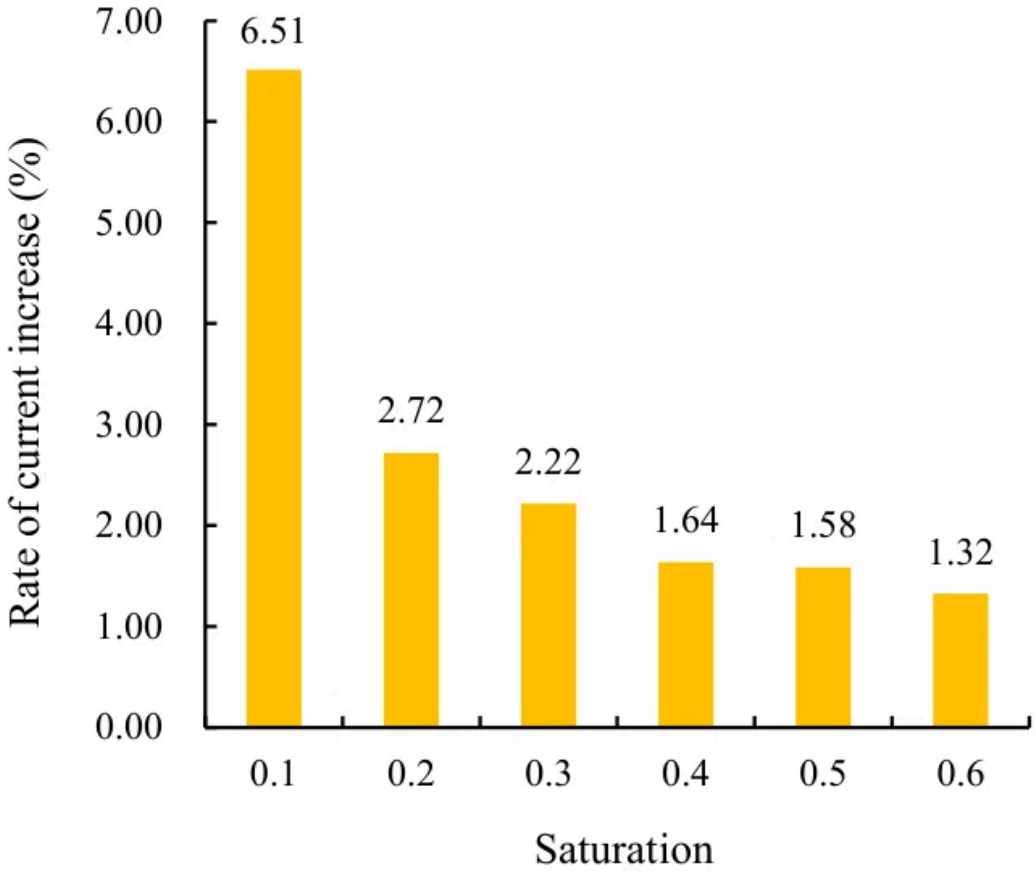


Figure 15. Ampacity increase rate vs. fine-sand backfill thickness.

4.3. Dynamic Current Limiting During Solar Radiation Periods

Solar irradiance elevates surface temperature and degrades cable heat dissipation, thereby reducing ampacity. Table 6 lists the quasi-steady ampacity ratio computed for each hourly irradiance value under varying red-bed soil saturations. For the night-time hours (6:00 p.m. to 6:00 a.m.) the imposed irradiance is zero and the steady-state solution therefore returns a ratio of 100%. As explained in Section 3.5, this value follows from solving each hour as an independent steady state and does not imply that full-load operation is permissible at night, because soil thermal inertia makes the cable at 1.2 m respond to the daily-mean irradiance, which is present throughout the night. The daytime values should be read as a conservative envelope of the solar-induced peak derating, and the table as a whole as a parametric sensitivity rather than a dispatch schedule. During the peak solar period from 10:00 a.m. to 2:00 p.m., the model indicates that the ampacity ratio should be restricted to about 80% to ensure safe operation. Based on Table 6, the time-dependent ampacity ratio can be fitted as shown in (18), where t denotes the clock time.

$$\begin{cases} I\% = 100 \quad 0 \le t \le 6,\ 18 < t < 24 \\ I\% = 0.5331t^2 - 12.795t + 155.83 \quad 6 < t \le 18 \end{cases} \tag{18}$$

5. Conclusions

This paper focuses on a 35 kV directly buried XLPE cable with a layered backfill structure of fine-sand cushion and red-bed soil. An electro-thermal-fluid multiphysics finite element ampacity evaluation model incorporating a saturation field and time-vary-

ing solar irradiance boundary is established. The main conclusions are as follows:

(1) A saturation-dependent thermal conductivity model based on the Johansen formula and on the coarse- and fine-grained Kersten branches is embedded in the finite-element equations as a spatial field variable, which replaces the homogeneous-soil assumption of conventional models. The simulation then reproduces the nonlinear dependence of ampacity on saturation: the ampacity increases by 58.5% when S_r rises from 0.1 to 0.3, by 11.5% from 0.3 to 0.6, and by only 5.5% from 0.6 to 1.0. Under identical homogeneous-soil conditions, the FEM ampacity agrees numerically with IEC 60287 within 3.4% on average (Section 2.6).

(2) The mechanism by which red-bed soil thermal resistance acts as the bottleneck for cable heat dissipation is revealed. Comparison across the seven spatial saturation scenarios (Table 5 and Figure 12) bounds the ampacity between the fully saturated case (Case 1, maximum) and the completely dry case (Case 7, minimum); Cases 2 and 4, which share wet red-bed soil, give close ampacities, and sand saturation only slightly affects Cases 3 and 5 with dry red-bed soil. Dry red-bed soil (S_r = 0.3) reduces ampacity by approximately 15%, whereas desiccation of the near-cable fine-sand layer affects ampacity by less than 2%.

(3) Solar irradiance is introduced as a time-varying boundary condition into the computational model, enabling hourly evaluation of the solar-induced ampacity derating. Increasing irradiance from 0 to 1000 W/m^2 reduces ampacity by approximately 20%, so the noon-peak ampacity ratio should be restricted to about 80% (Table 6). Because a separate steady-state solution is computed at each instantaneous irradiance and soil thermal inertia is not resolved, these intra-day values are parametric steady-state bounds rather than predictions of the instantaneous conductor temperature: the daytime peak derating is conservative, whereas the night-time 100% values are method artifacts and not an operating schedule (Sections 2.7 and 3.5).

(4) Based on the simulation results, an operation control strategy is proposed, with quantified thresholds for red-bed soil saturation control: normal operation ($S_{r_red} \geq 0.6$), early warning ($0.3 \leq S_{r_red} < 0.6$), and emergency intervention ($S_{r_red} < 0.3$). A time-slot-based ampacity ratio formula driven by solar variation is also proposed in response to diurnal solar variation, providing an actionable decision-support tool for field operation and maintenance in Southwest China.

Author Contributions: Conceptualization, Z.M.; methodology, Z.M.; software, Z.M.; validation, W.Z. and Z.M.; formal analysis, Z.M.; investigation, Z.M.; resources, W.Z.; data curation, Z.M.; writing—original draft preparation, Z.M.; writing—review and editing, Z.M.; visualization, Z.M.; supervision, Z.M.; project administration, W.Z.; funding acquisition, W.Z. All authors have read and agreed to the published version of the manuscript.

Funding: This work was supported by the Science and Technology Project of PowerChina Huadong Engineering Co., Ltd. (HDY-CGHT33-20230080Y) and the Scientific Research Start-up Fund Project of Yunnan Agricultural University (KY2026-10).

Institutional Review Board Statement: Not applicable.

Informed Consent Statement: Not applicable.

Data Availability Statement: The original contributions presented in this study are included in the article. Further inquiries can be directed to the corresponding author.

Acknowledgments: During the preparation of this manuscript, the authors used AI Tencent Yuanbao V2.93.0 solely for the purpose of language translation of the full text. No AI-generated content was used in the formulation of original scientific results, analyses, or conclusions. All tech-

nical contributions and data interpretations are solely those of the authors. The translated content was rigorously reviewed and edited by the authors, who take full responsibility for the final publication.

Conflicts of Interest: Author Wenlong Zhang was employed by the company PowerChina Huadong Engineering Corporation Limited. The remaining authors declare that the research was conducted in the absence of any commercial or financial relationships that could be construed as a potential conflict of interest.

References

1. Ocłoń, P.; Cisek, P.; Rerak, M.; Taler, D.; Rao, R.V.; Vallati, A.; Pilarczyk, M. Thermal performance optimization of the underground power cable system by using a modified Jaya algorithm. *Int. J. Therm. Sci.* **2018**, *123*, 162–180. [Google Scholar] [CrossRef]
2. He, X.; Teh, J. Impacts of dynamic thermal rating systems on wind generations: A review. *Electr. Power Syst. Res.* **2024**, *233*, 110492. [Google Scholar] [CrossRef]
3. Gouda, O.E.; Darwish, M.M.F.; Thabet, A.; Lehtonen, M.; Osman, G.F.A. Enhancement of the underground cable current capacity by using nano-dielectrics. *Energy Sci. Eng.* **2024**, *12*, 3647–3662. [Google Scholar] [CrossRef]
4. Ocłoń, P. The effect of soil thermal conductivity and cable ampacity on the thermal performance and material costs of underground transmission line. *Energy* **2021**, *231*, 120803. [Google Scholar] [CrossRef]
5. Maximov, S.; Venegas, V.; Guardado, J.L.; Moreno, E.L.; López, R. Analysis of underground cable ampacity considering non-uniform soil temperature distributions. *Electr. Power Syst. Res.* **2016**, *132*, 22–29. [Google Scholar] [CrossRef]
6. Shabani, H.; Vahidi, B. A probabilistic approach for optimal power cable ampacity computation by considering uncertainty of parameters and economic constraints. *Int. J. Electr. Power Energy Syst.* **2019**, *106*, 432–443. [Google Scholar] [CrossRef]
7. *IEC 60287-1-1:2023*; Electric Cables—Calculation of the Current Rating—Part 1-1: Current Rating Equations (100% Load Factor) and Calculation of Losses—General. IEC: Geneva, Switzerland, 2023.
8. *IEC 60287-1-2:2023*; Electric Cables—Calculation of the Current Rating—Part 1-2: Current Rating Equations (100% Load Factor) and Calculations of Losses—Sheath Eddy Current Loss Factors for Two Circuits in Flat Formation. IEC: Geneva, Switzerland, 2023.
9. *IEC 60287-1-3:2023*; Electric Cables—Calculation of the Current Rating—Part 1-3: Current Rating Equations (100% Load Factor) and Calculation of Losses—Current Sharing Between Parallel Single-Core Cables and Calculation of Circulating Current Losses. IEC: Geneva, Switzerland, 2023.
10. *IEC 60287-2-1:2023*; Electric Cables—Calculation of the Current Rating—Part 2-1: Thermal Resistance—Calculation of Thermal Resistance. IEC: Geneva, Switzerland, 2023.
11. *IEC 60287-3-1:2017*; Electric Cables—Calculation of the Current Rating—Part 3-1: Operating Conditions—Site Reference Conditions. IEC: Geneva, Switzerland, 2017.
12. Sucurovic, M.; Klimenta, D.; Tasic, D. Correction of the IEC formula for the eddy-current loss factor: The case of single-core cables in trefoil formation with metallic screens bonded and earthed at one end. *Facta Univ. Electron. Energ.* **2024**, *37*, 391–408. [Google Scholar] [CrossRef]
13. Wang, P. Optimization for thermal rating method of high voltage cable considering the existence of air gap. *Electr. Power Syst. Res.* **2023**, *217*, 109151. [Google Scholar] [CrossRef]
14. Verschaffel-Drefke, C.; Schedel, M.; Balzer, C.; Hinrichsen, V.; Sass, I. Heat Dissipation in Variable Underground Power Cable Beddings: Experiences from a Real Scale Field Experiment. *Energies* **2021**, *14*, 7189. [Google Scholar] [CrossRef]
15. Aras, F.; Oysu, C.; Yilmaz, G. An assessment of the methods for calculating ampacity of underground power cables. *Electr. Power Compon. Syst.* **2005**, *33*, 1385–1402. [Google Scholar] [CrossRef]
16. Nahman, J.; Tanaskovic, M. Determination of the current carrying capacity of cables using the finite element method. *Electr. Power Syst. Res.* **2002**, *61*, 109–117. [Google Scholar] [CrossRef]
17. Nahman, J.; Tanaskovic, M. Calculation of the ampacity of medium voltage self-supporting cable bunch. *Electr. Power Syst. Res.* **2012**, *93*, 106–112. [Google Scholar] [CrossRef]
18. Enescu, D.; Colella, P.; Russo, A.; Porumb, R.F.; Seritan, G.C. Concepts and methods to assess the dynamic thermal rating of underground power cables. *Energies* **2021**, *14*, 2591. [Google Scholar] [CrossRef]
19. *IEC TR 62095:2003*; Electric cables—Calculations for Current Ratings—Finite Element Method. IEC: Geneva, Switzerland, 2003.

20. Quan, L.; Fu, C.; Si, W.; Yang, J.; Wang, Q. Numerical study of heat transfer in underground power cable system. *Energy Procedia* **2019**, *158*, 5317–5322. [Google Scholar] [CrossRef]
21. Nie, Y.; Chen, D.; Zheng, S.; Xu, X.; Wang, X.; Wu, Z. Simulation and calculation of temperature field and current-carrying capacity of power cables under different laying methods. *Energies* **2024**, *17*, 4611. [Google Scholar] [CrossRef]
22. Kim, Y.-S.; Nguyen Cong, H.; Dinh, B.H.; Kim, H.-K. Effect of ambient air and ground temperatures on heat transfer in underground power cable system buried in newly developed cable bedding material. *Geothermics* **2025**, *125*, 103151. [Google Scholar] [CrossRef]
23. Hu, R.; Liu, G.; Xu, Z.; Wang, P.; Zeng, H.; Ye, W. Improved thermal analysis for three-core cable under unbalanced three-phase loads. *Electr. Power Syst. Res.* **2023**, *216*, 108964. [Google Scholar] [CrossRef]
24. Zhang, Y.; Chen, X.; Zhang, H.; Liu, J.; Zhang, C.; Jiao, J. Analysis on the Temperature Field and the Ampacity of XLPE Submarine HV Cable Based on Electro-Thermal-Flow Multiphysics Coupling Simulation. *Polymers* **2020**, *12*, 952. [Google Scholar] [CrossRef]
25. Chen, W.; Zhou, M.; Yan, X.; Li, Z.; Lin, X. Study on electromagnetic-fluid-temperature multiphysics field coupling model for drum of mine cable winding truck. *Trans. Electr. Mach. Syst.* **2021**, *5*, 133–142. [Google Scholar] [CrossRef]
26. Klimenta, D.; Perović, B.; Klimenta, J.; Jevtić, M.; Milovanović, M.; Krstić, I. Modelling the thermal effect of solar radiation on the ampacity of a low voltage underground cable. *Int. J. Therm. Sci.* **2018**, *134*, 507–516. [Google Scholar] [CrossRef]
27. Zhang, W.; Ma, Z. A Novel Dynamic Ampacity Assessment Method for Direct Burial Cables Based on an Electro-Thermal-Fluid Multiphysics Coupling Model. *Energies* **2025**, *18*, 6271. [Google Scholar] [CrossRef]
28. Bustamante, S.; Mínguez, R.; Arroyo, A.; Manana, M.; Laso, A.; Castro, P.; Martinez, R. Thermal behaviour of medium-voltage underground cables under high-load operating conditions. *Appl. Therm. Eng.* **2019**, *156*, 444–452. [Google Scholar] [CrossRef]
29. Shazly, J.H.; Mostafa, M.A.; Ibrahim, D.K.; Abo El Zahab, E.E. Thermal analysis of high-voltage cables with several types of insulation for different configurations in the presence of harmonics. *IET Gener. Transm. Distrib.* **2017**, *11*, 3439–3448. [Google Scholar] [CrossRef]
30. Möbius, P.; Michael, L.-H.; Plenz, M.; Schräder, J.; Schulz, D. Energy cable ampacity: Impact of seasonal and climate-related changes. *Renew. Sustain. Energy Rev.* **2025**, *212*, 115348. [Google Scholar] [CrossRef]
31. Maher, R.; El-Faraskoury, A.; Attia, M.A.; Emarah, A. Investigation of cable current carrying capacity improvement and its effects on transmit power between Egypt and Saudi Arabia project. *e-Prime-Adv. Electr. Eng. Electron. Energy* **2024**, *8*, 100579. [Google Scholar] [CrossRef]
32. Stojanović, M.; Klimenta, J.; Panić, M.; Klimenta, D.; Tasić, D.; Milovanović, M.; Perović, B. Thermal aging management of underground power cables in electricity distribution networks: A FEM-based Arrhenius analysis of the hot spot effect. *Electr. Eng.* **2023**, *105*, 647–662. [Google Scholar] [CrossRef]
33. Ocłoń, P.; Pobędza, J.; Walczak, P.; Cisek, P.; Vallati, A. Experimental validation of a heat transfer model in underground power cable systems. *Energies* **2020**, *13*, 1747. [Google Scholar] [CrossRef]
34. Różański, A.; Kaczmarek, N. Empirical and theoretical models for prediction of soil thermal conductivity: A review and critical assessment. *Stud. Geotech. Mech.* **2020**, *42*, 330–340. [Google Scholar] [CrossRef]
35. Wu, Y.-H.; Wu, Y.-F.; Fan, L.-W.; Yu, Z.-T.; Khodadadi, J.M. Thermal conductivity of soil: A review on the vast experimental data and predictive models. *Int. J. Therm. Sci.* **2025**, *208*, 109486. [Google Scholar] [CrossRef]
36. Smits, K.M.; Sakaki, T.; Limsuwat, A.; Illangasekare, T.H. Thermal Conductivity of Sands under Varying Moisture and Porosity in Drainage–Wetting Cycles. *Vadose Zone J.* **2010**, *9*, 172–180. [Google Scholar] [CrossRef]
37. Cai, Z.-L.; Li, Z.-L.; Meng, Y.-D.; Tian, S.-C.; Zhou, J.-W.; Tian, B. Predicting the thermal conductivity of red-bed soil based on multiphase medium. *Case Stud. Therm. Eng.* **2026**, *79*, 107804. [Google Scholar] [CrossRef]
38. NASA POWER|Data Access Viewer (DAV). Available online: https://power.larc.nasa.gov/data-access-viewer/ (accessed on 13 November 2026).
39. Guo, Q.; Liu, X. Evaluation and Optimization Design for Microclimate Comfort of Traditional Village Squares Based on Extension Correlation Function. *J. Environ. Public Health* **2022**, *2022*, 6106463. [Google Scholar] [CrossRef]

Disclaimer/Publisher's Note: The statements, opinions and data contained in all publications are solely those of the individual author(s) and contributor(s) and not of MDPI and/or the editor(s). MDPI and/or the editor(s) disclaim responsibility for any injury to people or property resulting from any ideas, methods, instructions or products referred to in the content.